Mechanical Systems and Signal Processing 230 (2025) 112664

Contents lists available at ScienceDirect

Mechanical Systems and Signal Processing

journal homepage: www.elsevier.com/locate/ymssp

Identification of nonlinear dynamic parameters of thrust bearings in rotating machines: Modelling of axial Sub-Synchronous vibration and experimental verification ☆

Ludovico Dassi *, Steven Chatterton, Paolo Pennacchi

Department of Mechanical Engineering, Politecnico di Milano, Via La Masa 1, 20156 Milan, Italy

ARTICLE INFO

Communicated by Spilios Fassois

Keywords:
Axial sub-synchronous vibration
Oil lubricated thrust bearing
Nonlinear dynamics
Structural integrity
Large rotating machines
Lubrication
Rotordynamics

ABSTRACT

Axial Sub-Synchronous Vibration (SSV) is an uncommon phenomenon that occurs in turbomachines. Specifically in compressors and large gas turbines equipped with double-sided, oil-lubricated thrust bearings. This phenomenon manifests as high-amplitude vibration which extends throughout the entire machine axial clearance. Consequently, the structural integrity of the machinery can be compromised, as the SSV can lead to detrimental effects such as fatigue cracks, seal abrasion, and fretting on bearings. This vibration develops unpredictably, with sudden amplitude jumps related to operational parameters such as active power, axial clearance adjustments, and lubricating oil temperature. While the literature extensively discusses potential causes, often linking vibration levels to fluid film instabilities on the reverse side of thrust bearings, this theory does not account for all observed cases. To understand the problem, the nonlinear behaviour of the oil film in the thrust bearing is analysed by solving the well-known Reynolds equation. The thrust force on the bearing collar is calculated and used to create a simplified axial model of the machine. Time integration and Harmonic balance methods are used to study the nonlinear dynamics, to identify the bifurcation region, and to perform sensitivity analyses by varying operational parameters. This phenomenon usually amplifies the vibration induced by the coupling between axial-lateral vibration, related to the thrust bearing collar. The proposed model, applied to a well-known example in the literature, offers insights into mitigating the adverse effects of axial SSV and improving the reliability of turbomachines.

Nomenclature

A_n	*Surface area of pad "n" [m^2]*
A_0	*amplitude of the dynamic force [N]*
cl	*axial clearance of thrust bearing [micron]*
C_{tot}	*linearized damping coefficient [N/m*s]*
D_{collar}	*outer diameter of thrust collar [mm]*
F^i_{brg}	*total axial dynamic force generated by bearing "i" [N]*
F^c_{dir}	*axial damping force on direct side of bearing "i" [N]*
F^c_{rev}	*axial damping force on reverse side of bearing "i" [N]*

(*continued on next page*)

☆ This article is part of a special issue entitled: 'Prof. Mottershead' published in Mechanical Systems and Signal Processing.

* Corresponding author.
E-mail address: ludovico.dassi@polimi.it (L. Dassi).

https://doi.org/10.1016/j.ymssp.2025.112664
Received 1 November 2024; Received in revised form 25 February 2025; Accepted 27 March 2025
Available online 3 April 2025
0888-3270/

Nomenclature (*continued*)

F^{k}_{dir}	*axial stiffness force on direct side of bearing "i" [N]*
F^{k}_{rev}	*axial stiffness force on reverse side of bearing "i" [N]*
F^{ik}_{tot}	*net stiffness axial force generated by bearing "i" [N]*
F^{ic}_{tot}	*net damping force generated by bearing "i" [N]*
F_{dyn}	*dynamic force in axial direction [N]*
F_{stat}	*static force in axial direction [N]*
h	*oil film thickness on bearing pad [micron]*
H	*Harmonic order [-]*
HB	*Harmonic Balance*
J^{i}_{pad}	*moment of inertia of the pad rotation around the pivot for bearing "i" [N·m]*
K^{i}_{dir}	*thrust bearing tilting stiffness direct side [Nm/rad]*
K^{i}_{rev}	*thrust bearing tilting stiffness reverse side[Nm/rad]*
N_{pads}	*Number of pads on direct or reverse side [-]*
μ	*local lubricant dynamic viscosity [Pa·s]*
ω	*pulsation frequency of the dynamic force [rad/s]*
Ω	*shaft rotating speed [rpm]*
P_{oil}	*local normal pressure generated by oil film on pad surface [MPa]*
Q_n	*Fourier coefficient of "i" harmonics [-]*
R_i	*Residual of HB related to "i" harmonics [-]*
R_{geom}	*geometric proportion between the thrust collar outer diameter and the shaft length [-]*
SSV	*sub-synchronous vibration*
U	*sliding velocity on bearing pad [m/s]*
w	*squeezing velocity perpendicular to the pad surface [m/s]*
x_{shaft}	*axial position of thrust collar [micron]*
$\dot{x}_{shaft}$	*axial velocity of thrust collar [m/s]*
$02p$	*vibration amplitude zero-to-peak*
$p2p$	*vibration amplitude peak-to-peak*

1. Introduction

In today energy scenario, turbomachines are required to work in a wide range of operating conditions, not only at rated power. Fast changes in the operating parameters, such as: active load, flow rate of the processed fluid, and rotating speed can occur often. This usually implies a broadband excitation of the system dynamic response [1,2]. This is the case of high amplitude axial vibration, which can suddenly arise in large turbomachines. The unpredictable system response and the possible onset of trip condition increase the importance of the topic [3]. Even though the topic is rarely discussed in the literature, the axial SSV phenomenon has a relevant industrial importance, and it finds evidence both in small and large rotating machines, as stated in [4,5]. An interesting study about axial sub-synchronous vibration has been reported in the literature by DeCamillo [6], but the phenomenon remains insufficiently explored. Although the literature case in reference [6] is somewhat dated, it remains the most comprehensive analysis available for experimental validation about this topic. Machines equipped with double-sided oil-lubricated thrust bearings [7], especially those operating under low axial loads, are particularly vulnerable to this issue. The amplitude of this vibration often reaches the full axial clearance, creating a serious hazard for the mechanical integrity of the system and leading to possible damages, such as seal rubbing, fretting of the bearing pads, fatigue, or even seizure of the pivots [8,9].

The occurrence of axial SSV under specific operating conditions highlights the complexity of axial dynamics in turbomachinery [10]. To correctly address the topic, several forces should be considered in the analysis, mainly the external ones but also those generated by the oil film within the thrust bearing, as stated in [11]. In particular, several excitation sources can occur, for example the turbulent motion of the lubricant, incomplete oil filling of the bearing film and pad fluttering.

Several explanations have been proposed in the literature to identify the root causes of axial SSV. Gardner [12] and Wu [13] suggested that fluid dynamic instabilities within the oil film wedge, caused by improper oil flow, could be a contributing factor. Oil flow rate, whether insufficient or excessive, could alter the stability of the lubricating film, leading oil-film rapture, which manifest as sub-synchronous vibration. These instabilities, occurring at the microscopic level within the thin oil wedge, could create forces that drive the axial motion. Mikula [14], on the other hand, focused on the possible fluttering of slack pads on the unloaded side of the thrust bearing. Pad fluttering, a form of mechanical instability, occurs when the thrust bearing pads, no longer tightly compressed by the axial load, begin to oscillate around the pivot. This flutter could introduce additional vibrational forces into the system, generating the SSV issue. Despite these case-related explanations, a comprehensive understanding remains unavailable, as the proposed theories do not fully explain all the observed cases. More recent studies by Peixoto [15] and Ishimoto [16] highlighted the potential coupling between axial and radial vibration in automotive turbochargers, with self-excited sub-synchronous vibration being linked to interactions between out-of-plane modes [17,18]. In these cases, shaft bending modes were radially excited at their natural frequencies [19], and the thrust collar couples radial oscillations into axial force pulsations. This model had shown significant results in automotive applications, particularly in high-speed turbochargers, where axial sub-synchronous vibrations have been observed and studied in detail.

However, while the coupled model has been effective in smaller automotive systems, its application to large turbomachinery is less clear. The dynamics in larger systems introduce additional complexities, such as higher mass, larger operational load, and different oil film behaviour, making direct comparison challenging, as discussed in [20]. The need for expanding the research in this area is interesting, especially as newest turbomachines push the operational limits, increasing the risk of axial SSV events. By reviewing the literature, a large variety of rotating machines suffer of axial SSV, namely: large gas turbines for power generation (power $>$ 100 MW) [21], small turbochargers for automotive sector [17] and flywheels for electric grid stabilization [22,23]. The dimension of the thrust bearing collar seems not to be strictly correlated to the occurrence of the phenomenon. The geometric proportion (R) between the thrust collar outer diameter and the shaft length $R_{geom} = \frac{D_{collar}}{L_{shaft}}$ has been investigated as a possible explanation of the SSV occurrence for several machines documented in the literature. The results of the analysis are shown in Table 1.

Although the DeCamillo test rig exhibits a relatively larger thrust collar dimension, our analysis did not reveal a significant correlation between the thrust collar dimension ratio and the occurrence of axial SSV. Even though the considered machines have a variable geometry ratio, axial SSV occurrence is documented for all of them. This suggests that the coupling of axial and lateral vibrations is not strongly influenced by the thrust collar size relative to the shaft length.

Fig. 1 presents a representative waterfall diagram of axial vibrations in a rotating machine equipped with a double-sided oil-lubricated thrust bearing. Data comes from a real machine affected by the axial SSV issue, recorded on-site and processed using filtering and frequency analysis in Matlab R2023b. The case study is significant because the most relevant nonlinear features of axial SSV are clearly visible. First of all, the vibration occurs at a frequency much lower than the rotating speed (1X). Usually, as reported in the literature, the frequency component is about $\sim$ 0.2X, but this indication is not fix and it highly depends on the considered machine. The measured SSV vibration is mainly in axial direction, but it can be easily found also in lateral direction. This aspect is a significant hint about the coupling between lateral and axial vibrations, generated by the collar motion. In the literature, Lie [24] and Kiuchi [25] widely discussed the topic. The frequency of the axial SSV also appears to slightly shift depending on the thrust load applied to the axial bearing. As the load increases, the frequency of the SSV generally increases, but when the load reaches a critical threshold, the vibrations completely disappear. This dependency on load is one of the more representative features of axial SSV, as it states a highly nonlinear relationship between operational parameters and vibrational response.

Another important feature of axial SSV is the sudden and sharp changes in the vibration amplitude. These typically occur in response to even slight changes in operational parameters of the machine, such as thrust load, oil flow rate, inlet temperature, and axial clearance. These abrupt shifts can be challenging to predict, and the phenomenon shows a form of hysteresis, with different starting and stopping conditions depending on whether the machine is increasing or decreasing the output power. This hysteresis behaviour suggests that once initiated, the sub-synchronous vibration may persist even after the original triggering conditions have changed.

By renewing the literature, DeCamillo [6] proposed that these jumps in amplitude could be linked to the resonance within the axial system. Resonance conditions, where natural frequencies of the system aligned with excitation frequencies, could account for the sudden amplification of vibration. The present work has the goal to investigate this hypothesis, examining how nonlinear axial dynamics, driven by fluid forces in the thrust bearing oil film, can explain several features of the SSV. Furthermore, amplitude jumps, and frequency shifts can be reasonably explained, as discussed in details by Chatzisavvas in [19].

Fig. 2 is just a qualitative sketch of the typical steady-state dynamic response of a nonlinear system, created by mean of Matlab R2023b. It does not refer to any real case but it is useful to highlight and discuss the main features of the system. The frequency of the excitation force is swept, showing how the peak of dynamic amplification is altered. The resulting shape is the so called “backbone curve”, the peak can be more or less bended depending on the degree of system nonlinearity. For this field, thrust bearing has usually a stiffening behaviour by increasing the applied load, so the curve is bent to the right side. The highlighted region is the bi-stability region, where sudden jumps in vibration can occur even though the two solutions are always stable.

Harmonic balance and Time integration methos are usually used to solve the nonlinear axial dynamics of the system model. The former approach is useful to create sensitivity maps to the operating parameters in steady-state conditions. The latter approach gives interesting insights about sudden amplitude jumps and hysteretic behaviour.

Harmonic balance method is a powerful tool for studying nonlinear axial dynamics, which allows an efficient computation of steady-state responses in systems subjected to periodic excitation [26]. The HB method transforms the constitutive nonlinear differential equations of the system from time domain into the frequency domain, where they can be easily solved. The tentative solution has the form of a truncated Fourier series, and it is plugged in the constitutive equation of motion. The balancing of the harmonics is performed by grouping the similar harmonic terms and by imposing the equality of the respective Fourier coefficients. At the end, a system of algebraic equations is obtained, which is effectively solved by standard numerical techniques, such as Newton solver [27,28]. The Harmonic balance method has several advantages, including a significant reduction in the computational effort compared to time-domain integration. It allows for quicker evaluations of system response over a wide range of parameter values. It also enables the generation of sensitivity maps of the system behaviour for changes in the system parameters, such as thrust load, oil flow rate, bearing axial clearance and shaft rotational speed. However, the Harmonic balance method is limited to periodic and steady-state conditions, and it is not suitable for transient conditions. Despite this limitation, Alevras in [29] successfully used the Harmonic balance approach to predict the behaviour of highly nonlinear systems, demonstrating its applicability in real-world engineering

Table 1
Investigation on relative thrust collar dimension for several machines experiencing axial SSV.

Machine type	Literature source	D_{collar}	R_{geom}
De Camillo lab test rig	[6]	267 mm	R = 0.16
Large flywheel	[22,23]	350 mm	R = 0.14
Large gas turbine	[21]	1300 mm	R = 0.10
Automotive turbocharger	[15]	10 mm	R = 0.08

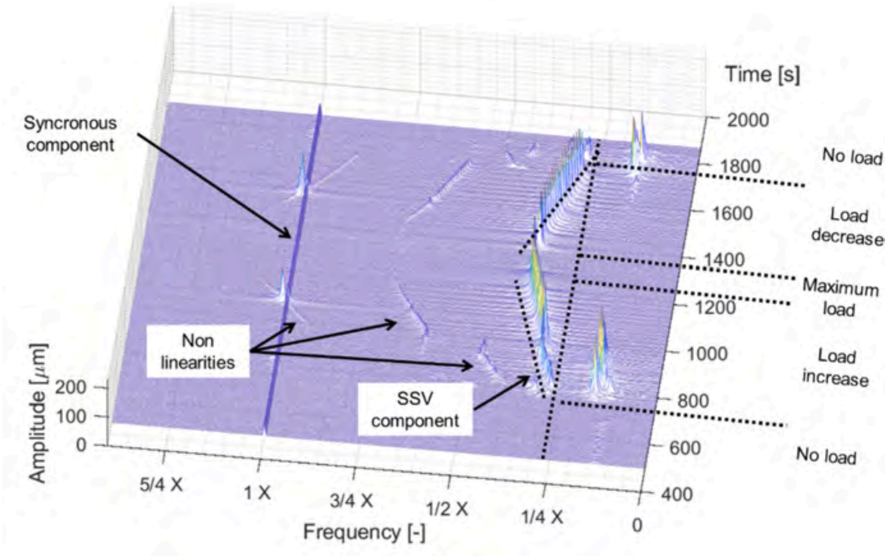

Fig. 1. Representative real case waterfall plot of an axial SSV vibration for a real rotating machine. Interesting to notice the SSV component, the nonlinearities signatures, the frequency shift and the amplitude jumps.

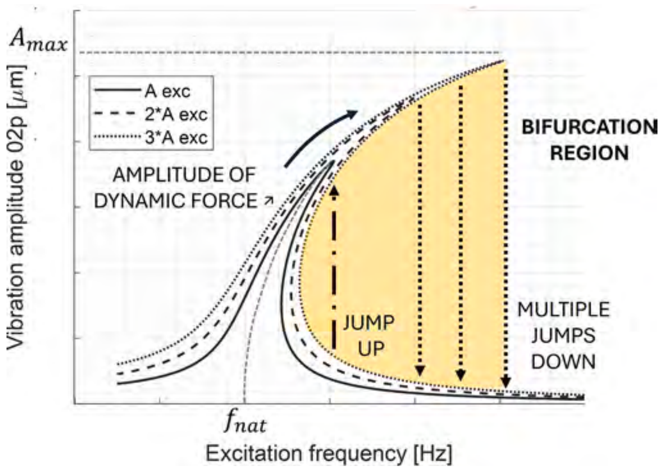

Fig. 2. Qualitative sketch of the backbone curve, this example represents the typical steady-state dynamic amplification of a nonlinear system; featuring stiffening behaviour, a bi-stable region, and amplitude jumps.

problems.

Time integration solvers offer a systematic approach to discretize continuous differential equations [30]. The solution of the equation of motion is approximated over successive time steps. Among the most widely adopted techniques for this purpose, Runge-Kutta adaptive solvers, which belong to the family of explicit Time integration schemes, are well-suited for systems with low order of stiffness and complex non-linearities [31,32]. The adaptive step-size control allows an efficient handling of systems in which rapid changes in the solution demand dynamic adjustment of computational effort. Its robustness makes it particularly appropriate for handling the inherent nonlinearities in the equations of motion, where small errors can lead to significant deviations in results. When dealing with adaptive solvers, it is always important to lowering the maximum frequency of the external acting force to keep the time-step sufficiently high. Usually, it is convenient to perform low pass filtering of the excitation force, whenever possible.

The aim of this study is to increase the knowledge of axial SSV. Although the nonlinear axial dynamics in rotating machinery with oil-lubricated thrust bearings is often neglected, it can provide some significant insights into the unpredictable behaviour of the considered vibration. Great interest is given to the experimental analysis reported in [6], where axial SSV was successfully reproduced under controlled conditions. The corresponding numerical model of the system is now implemented, fluid dynamic forces of the thrust bearings are firstly calculated by mean of Reynolds equation and they are used to implement the nonlinear axial dynamics model of the test rig. The experimental data given in the literature are used for validating the proposed model. Additionally, the potential correlation between the rotor bending modes and the excitation force in the axial direction is preliminary discussed.

This paper is structured as follows: Section 2 explains the geometry of test-rig in [6], used as reference case study. Particular attention is given to the geometry of the double-sided oil-lubricated thrust bearing and the estimation of the fluid dynamic forces. Section 3 introduces the numerical model developed to study the nonlinear axial dynamics of the system. The two mathematical solvers used to predict the system response are here discussed (Harmonic balance and Time integration). A simplified lateral dynamics model is briefly introduced to investigate the correlation between radial and axial dynamics. Section 4 discusses the numerical results of the bearing forces. Section 5 presents the main numerical results of the axial dynamics, and it compares them with the experimental findings. Finally, Section 6 outlines the key conclusions of this research and the future developments on this topic.

2. Test-rig and double-sided thrust bearing geometries

2.1. Geometry of the rotor

The experimental test rig examined in this study, originally described in [6] and further elaborated by Wilkes et al. in [33], was specifically designed to investigate the behaviour of thrust bearings under controlled conditions. One of the significant advantages of this setup was its ability to eliminate typical aero-excitation forces that are often present in industrial rotating machines. Despite the exclusion of these forces, the rig was successful in reproducing axial subsyncronous vibrations (SSV), indicating that these vibrations could originate from factors inherent to the thrust bearings themselves. This finding contradicted the conventional hypothesis that axial SSV are primarily caused by aero forces.

Although the literature case in reference [6] is somewhat dated, it remains the most comprehensive analysis available for experimental validation on this topic. In particular, it is unique in that axial SSV are reproduced in a highly controlled environment where the operating conditions can be adjusted one at a time. This makes the results particularly valuable in understanding the underlying mechanisms of axial SSV and how they can be influenced by specific variables.

The test rig discussed in [6] is now presented. The rig was powered by a variable-speed gas turbine, which drove a central rotating shaft capable of speeds ranging from 6,000 to 15,000 rpm. The turbine was mechanically isolated from the main shaft by a fully flexible coupling, ensuring that no turbine-induced forces were directly transmitted to the shaft. The configuration of the main shaft was illustrated in Fig. 3, and its key geometrical dimensions are reported in Table 2. The shaft was supported at both ends by oil-lubricated tilting-pad journal bearings, ensuring stability during high-speed operations.

The geometry of the system was comprehensively detailed by Wilkes in [33]. The core of the test rig was composed of two double-sided, oil-lubricated thrust bearings, each with a shaft collar. These thrust bearings played a crucial role in investigating axial SSV and allow for various configurations. The first thrust bearing was mounted in an adjustable casing, enabling the application of precise axial loads via an external hydraulic system. This casing could also be locked to the ground for tests conducted under no-load conditions. The second thrust bearing was fixed rigidly to the baseplate, carrying the full axial load during testing. The design of the test rig also allowed for the adjustment of multiple operating parameters, such as rotational speed, axial load, axial clearance, oil inlet temperature, and oil flow rate. Moreover, the modular design of the rig allowed for the removal or replacement of thrust bearings to accommodate specific test requirements.

The testing procedure used in DeCamillo's study focused on systematically varying the operating conditions to observe their effects on axial SSV. The rig was operated over a wide range of speeds, from 6,000 to 15,000 rpm, and oil flow capacities, up to 270 l/min. Axial clearances were adjusted between 260 and 600 μm, while oil inlet temperatures ranged from 40 °C to 75 °C. The experiments were conducted in several phases. Initially, tests were performed under no axial load, with incremental adjustments to axial clearances and oil flow rates to identify conditions that induced axial SSV. Vibrations were monitored using axial proximity probes, and frequency spectra were analysed to detect subsyncronous vibration signatures. During subsequent phases, axial loads were applied using the hydraulic system, and the effects on vibration amplitudes were recorded. Notably, axial SSV tended to diminish or disappear when the

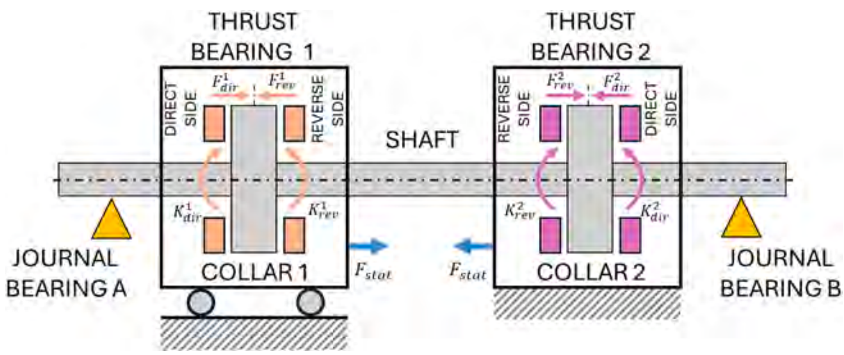

Fig. 3. Schematic of the experimental test rig for thrust bearings where axial SSV was reproduced in [6]. Both geometries and main acting forces are shown.

Table 2
Key dimensions and characteristics of the test rig in the literature case [6].

Property	Dimension	Unit
Shaft length	1700	mm
Shaft diameter	122	mm
Collar diameter	292	mm
Rotor mass	213	kg
Rotating speed	6000–15000	rpm
Axial load	0–10	kN

load exceeded a critical threshold, which is consistent with nowadays field observations.

The study also included parameter sensitivity tests, where key parameters such as oil flow rate and axial clearance were systematically varied. The goal was to map their influence on the onset and intensity of axial SSV, with waterfall plots being used to visualize vibration behaviour across the operating range. This rigorous testing methodology provided valuable insights into the dynamics of axial SSV, revealing that these vibrations could be triggered by specific combinations of low axial loads, reduced axial clearance, and moderate oil flow rates. These findings underscored the importance of bearing stiffness and lubrication dynamics in the occurrence of axial SSV.

2.2. *Geometry of the double-sided thrust bearing*

The thrust bearings tested in the test rig in [6] were conventional flooded designs Tilting Pad Thrust Bearing (TPTB). Each bearing was equipped with proximity probes and load cells to measure hydrodynamic film forces and pad vibrations. High-resolution vibration data were collected through data acquisition systems, allowing for precise frequency analysis. The geometry of the thrust bearings varied between bearings 1 and 2. Bearing 1 features a 6-pad TPTB with a 60 % offset pivot and LEG lubrication. Its outer diameter measured 267 mm, while the inner diameter was 134 mm, with both the direct and reverse sides provided with the same pad geometry. The lubricant used was ISOVG32 oil, a common choice for ordinary turbomachines. Bearing 2 had the same bearing diameters of bearing 1, but the number of pads changed to 8 and the pad length was adjusted to fit them circumferentially. A sketch of the thrust bearing geometry is shown in Fig. 4. The main geometrical specifications of the thrust bearings are listed in Table 3, and a detailed description of the bearing geometry can be found in [14] and [34].

3. Numerical model for nonlinear axial dynamics

In this section a numerical model is implemented to study the system nonlinear axial dynamics. The rotor is simplified as a lumped mass which moves horizontally while the thrust bearings are the main nonlinear contributions. Firstly, the fluid dynamic forces of the thrust bearings are modelled by mean of the lubrication theory Reynolds equation.

3.1. *Estimation of thrust bearing fluid dynamic forces*

First of all, the oil film forces have been obtained by modelling the oil film wedge in the double-sided oil-lubricated thrust bearing. Reynolds equation (Equation (1) is solved for two considered pad layouts using a finite difference method. The formulation accounts

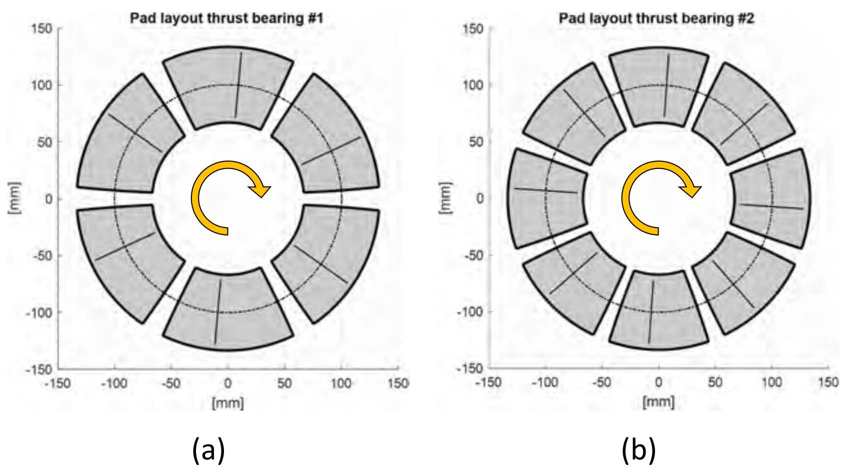

Fig. 4. Pad layout of thrust bearing #1 (a) and thrust bearing #2 (b), pivot is highlighted for each pad, the direction of collar rotation is shown for clarity. Geometry from [6].

Table 3
Key geometrical characteristics of the analysed thrust bearings, data from [6].

Property	Bearing #1	Bearing #2	Unit
Pads number	6	8	–
Lubrication type	LEG	LEG	–
Pivot offset	0.6	0.6	%
Clearance	260–600	260–600	μm
Outer diameter	267	267	mm
Inner diameter	134	134	mm
Pad angle	50.88	38.18	deg
Pad width	66.5	66.5	mm
J_{pad}	1.29110^{-3}	6.76310^{-4}	Kg/m^2

for the influence of temperature on the oil physical properties, and it neglects the effect of centrifugal forces, as described in [23]. The analysis focuses on a single pad under the hypothesis of circumferential periodicity. In Equation (1), the variables r and θ represent the cylindrical coordinates, p is the local pressure, h denotes the oil film thickness, ω is the shaft rotational speed, μ the dynamic viscosity of the lubricant, which varies with the local oil temperature.

$$\frac{\partial}{\partial \mathrm{r}}\left(\mathrm{h}^3\frac{\partial \mathrm{p}}{\partial \mathrm{r}}\right)+\frac{\mathrm{h}^3}{\mathrm{r}}\frac{\partial \mathrm{p}}{\partial \mathrm{r}}+\frac{1}{\mathrm{r}^2}\frac{\partial}{\partial \theta}\left(\mathrm{h}^3\frac{\partial \mathrm{p}}{\partial \theta}\right)=6\,\mu\,\omega\frac{\partial \mathrm{h}}{\partial \theta} \tag{1}$$

Key inputs for the analysis include the pad geometric characteristics, the applied load on the pad surface, the inlet oil temperature at the leading edge, axial clearance, and shaft spinning speed. Given that the bearings under consideration are of the leading-edge-groove (LEG) type, each pad features a groove at the leading edge, introducing a flow of colder oil. To simplify the geometry, the analysis excludes the groove region and focuses only on the active pad surface, as the groove has a minimal effect on the dynamic pressure distribution. The inlet oil temperature is varied between 45 °C and 75 °C, and its impact on the results is quantified. A key assumption in this analysis is the use of the Reynolds equation, which simplifies the model by ignoring the effects of centrifugal inertia forces in the oil and the incomplete filling of the wedge. These factors become significant at high rotational speeds, since they can reduce the pressurization within the bearing.

The results of the analysis yield to surface maps, showing the distribution of pressure and temperature across the pad surface. By integrating the pressure distribution over the pad area, the relationship between the applied load and the collar position for each side of the thrust bearings can be obtained. The non-linear stiffness force $F^k_{dir/rev}$ generated in the oil film, on both the direct and reverse sides of the collar, is determined as the sum over all the pads and it is function of the collar displacement (x_{sha}), as expressed in Equation (2). The computed force is calculated by applying the static equilibrium to the collar.

$$F^k_{dir/rev}=\sum_{n=1}^{N_{pads}}\int_{A_n}P_{oil}dA=F^k_{dir/rev}(x_{sha}) \tag{2}$$

After determining the force–displacement relationship for each side of the bearing separately, the next step is to consider the effect of axial clearance (cl). The force for the reverse side of the bearing is shifted by the axial clearance and its sign is reversed to consider for the opposite direction (Equation (3).

$$F^k_{rev}=-F^k_{rev}(cl-x_{sha}) \tag{3}$$

These two force contributions are then summed up (Equation (4), and the resulting net axial load on the bearing is calculated as the difference between the forces produced by the two sides of the bearing. This method enables the creation of a coupled model that accounts for the two-directional reaction forces generated by the bearing due to axial displacement of the collar. The model also includes the pressurization effect induced by shaft rotation, under the previously mentioned hypothesis, namely no centrifugal force and complete oil wedge filling. An example of the non-linear stiffness force contributions on the bearing sides is shown in Fig. 10a while the net axial load is shown in Fig. 10b.

$$F^k_{tot}=F^k_{dir}(x_{sha})-F^k_{rev}(cl-x_{sha}) \tag{4}$$

A similar procedure is applied to calculate the nonlinear damping forces $F^c_{dir/rev}$, generated by the squeezing of the oil film wedge inside the thrust bearings. To compute the force, the collar axial position is changed discretely, and an infinitesimal squeezing velocity is applied to the collar. The amplitude of the applied squeezing velocity is chosen by convergence analysis. At the end, an approximation of the nonlinear squeezing force curve is calculated, according to Equation (5) and (6). The curve is valid under the simplification of low squeezing velocities. In other words, the force is linearized with respect to the velocity amplitude, but not with respect to the collar position. Consequently, the damping force can be expressed also as the product of the nonlinear damping coefficient C_{tot}, which depends only on the collar position, and the squeezing velocity (Equation 7). An example of the nonlinear damping coefficient trend is shown in Fig. 11. The axial analysis is performed under a range of operating conditions for the thrust bearings, including variations in axial load, axial clearance, inlet oil temperature, and shaft rotational speed. For each set of conditions, a unique force–displacement relationship is computed, allowing for a comprehensive understanding of the system behaviour.

$$F^c_{dir/rev} = \sum_{n=1}^{N_{pads}} \int_{A_n} P_{oil} dA = F^c_{dir/rev}(x_{sha}, \dot{x}_{sha}) \tag{5}$$

$$F^c_{tot} = F^c_{dir}\left(x_{sha}, \dot{x}_{sha}\right) - F^c_{rev}((cl - x_{sha}), -\dot{x}_{sha}) \tag{6}$$

$$F^c_{tot}\left(x_{sha}, \dot{x}_{sha}\right) \simeq F^c_{tot}(x_{sha}) = C_{tot}(x_{sha}) {}^{*} \dot{x}_{sha} \tag{7}$$

For studying the lateral dynamics of the rotor, the same procedure is applied to calculate the rotation stiffness associated to the thrust collar rotation ($K^i_{d,r}$). Each side of the thrust collar provides a tilting torque, which is computed by summing up the all the forces generated by the pads multiplied by the distance with respect to the rotation axis. The local oil film thickness at pivot now depends both on the axial position of the collar, and on the tilting angle of the collar. For search of brevity, the tilting stiffness is linearized around the collar equilibrium position for each case study.

3.2. Equation of motion for axial nonlinear dynamics

A fundamental step in this analysis involves the investigating of the rotor axial vibration due to the system axial nonlinearity. In the existing literature, axial sub-synchronous vibration typically occurred at a frequency near the first rigid body mode of the entire machine shaft. The central hypothesis of this research is that the amplitude of SSV can be significantly increased when it tunes with the natural frequency of the shaft first axial rigid body motion.

To test this hypothesis, a simplified nonlinear model is developed by considering a one-degree-of-freedom axial vibrating system subjected to non-linear forces. Specifically, the entire shaft is represented by a lumped mass, and the highly nonlinear forces transmitted between the shaft and the two thrust bearings are derived from the calculations in Section 3.1. The bearing nonlinear forces account for different contributions. Stiffness and damping forces depend on the collar position. A small amplitude dynamic excitation force is applied, and the system response is calculated. This methodology does not consider dynamic instability issues. A sketch illustrating this model is provided in Fig. 5.

The fundamental equation of motion governing the system is given in Equation (8). The second-order dynamic equation is composed by the inertia term ($m\ddot{x}_{sha}$) and the nonlinear forces generated by the two thrust bearings. For thrust bearing #1, the total force transmitted (F^1_{brg}) is the sum of the nonlinear stiffness force (F^{1k}_{tot}) and nonlinear damping force (F^{1c}_{tot}), further discussed in Section 3.1; the external static thrust load applied to the bearing housing (F_{stat}), and a sinusoidal perturbation force (F_{dyn}). The same methodology applies to thrust bearing #2, without the perturbation contribution.

$$m\ddot{x}_{sha} - F^1_{brg} + F^2_{brg} = 0 \tag{8}$$

$$with: \begin{cases} F^1_{brg} = F^{1k}_{tot} + F^{1c}_{tot} + (F_{stat} + F_{dyn}) \\ F^2_{brg} = F^{2k}_{tot} + F^{2c}_{tot} + F_{stat} \\ F_{dyn} = A_0 {}^{*} \sin(\omega t) \end{cases}$$

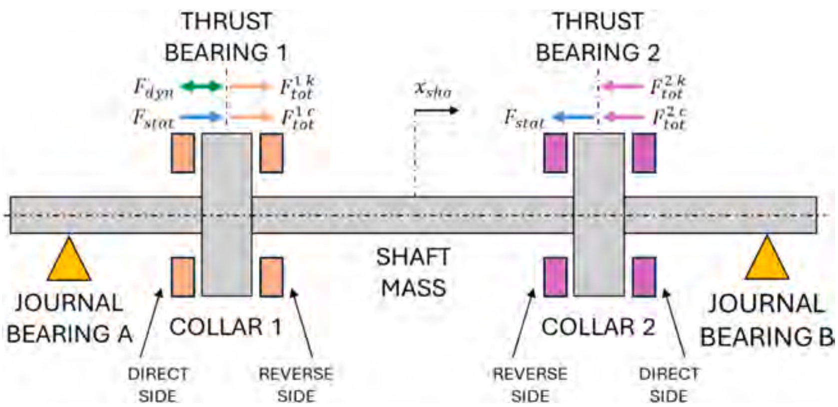

Fig. 5. Schematic of the single degree-of-freedom nonlinear system used for modelling nonlinear axial dynamics. Geometry layout comes from [6].

3.3. Harmonic balance solver

The system dynamics is mainly studied by using the Harmonic balance method for a general harmonic excitation, as shown in Equation (9). This approach reformulates the differential equation problem as a system of algebraic equations, where each row corresponds to a residual R_i. Each residual represents the difference between the tentative solution and the correct solution over one oscillation period. A harmonic order of $H = 7$ is used for the tentative solution, meaning the approximate solution is expressed as a sum of seven harmonics in a truncated Fourier series. In the frequency domain, each harmonic amplitude is determined by the corresponding Fourier expansion coefficient Q_i, which are iteratively adjusted to approximate the correct solution. The thrust bearing nonlinear forces are modelled using the Alternating Time Frequency (ATF) method.

$$HB = \begin{bmatrix} R_0(Q_0, Q_1, \cdots Q_H) = 0 \\ R_1(Q_0, Q_1, \cdots Q_H) = 0 \\ \vdots \\ R_H(Q_0, Q_1, \cdots Q_H) = 0 \end{bmatrix}_{n(2H+1)} \tag{9}$$

The system solution is computed over a frequency range of [60 ÷ 270 Hz]. The procedure is repeated under various operating conditions of the thrust bearing, as detailed in Section 3.2, with the corresponding force–displacement relationships serving as input for the HB analysis. For each case, the backbone curve is derived, and the bifurcation region is identified. The bifurcation zone refers to the parameter range where two or more stable solutions coexist, which is why it is also called as bi-stable region. According to existing literature, bi-stability plays a crucial role in defining the jump phenomenon in vibration amplitude [24]. When bifurcation occurs, it is important to use techniques of path continuation to correctly catch all the three branches of the backbone curve.

3.4. Time integration solver

The main limitation of Harmonic balance method is its applicability only for steady-state and periodic solutions. Transient conditions cannot be addressed. For this reason, Time integration approach is also considered. The solver used in a Runge-Kutta approach with adaptive time step. This solver is applied to the same dynamic equation of the system (Equation (8), nonlinear bearing forces are calculated as previous discussed. This approach is useful to mimic the system transient response when the applied operating parameters change, in particular great attention is given to the case of changing static thrust load. This condition is common in real machines and widely discussed in the literature.

3.5. Considerations about excitation sources

The more challenging part of the axial SSV modelling is the definition of the external excitation force. The literature presents many possible explanations, but the researchers do not agree on them. For the sake of generality, the external force is here considered as a monotone harmonic force with a given frequency and amplitude. The frequency of the force should be that one related to the physical phenomenon considered, while the amplitude is tuned in order to reach a reasonable system response, similar to that one experienced in [6].

A possible excitation source comes from the coupling between lateral and axial dynamics due to the tilting motion of the thrust collar. This explanation is widely discussed in the literature related to automotive turbochargers. Moreover, this explains why it is commonly possible to catch the axial SSV signature also in radial directions. A sketch of the thrust collar motion and its coupling effect between axial and lateral dynamics is shown in Fig. 6. A simple explanation of the phenomenon is that even though the collar rotation

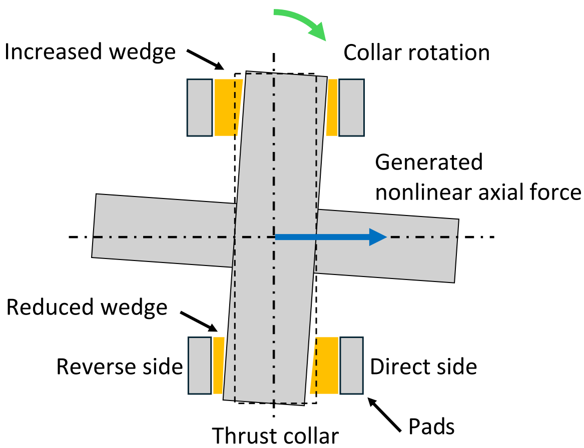

Fig. 6. Sketch of the coupling effect of thrust collar for axial and radial dynamics.

has a symmetric effect on the oil film wedge squeezing, then the resulting forces are not balanced due to the nonlinearity of the given forces. As a result, a net axial excitation force is generated with the same frequency of the collar tilting motion.

In this research only the natural frequencies related to the first bending modes of the test rig are investigated. A simplified and linearized model for the lateral dynamics is developed with the aim of determining whether any bending modes of the test rig have natural frequencies that are similar with the axial resonance.

3.6. Finite element rotordynamic bending model

For this analysis, a standard Finite Beam Element (FE) rotordynamic model of the shaft is employed, focusing on the rotor lateral vibrations. The dynamic coefficients of the journal bearings are sourced from existing literature, while the tilting stiffness contributed by each thrust bearing ($K^i_{d,r}$) is computed and included into the model. Fig. 7 provides a schematic representation of the resulting FE model, detailing the mass and stiffness diameters along the rotor length.

Specifically, the top plot shows the mass diameters distributed along the rotor. These diameters generally align with the physical dimensions of the shaft and are larger at the thrust collars. This mass distribution is essential for accurately defining the rotor inertial properties, directly impacting the dynamic response of the system. The bottom plot depicts the bending stiffness diameters along the rotor. For each finite element a beam Eulero-Bernulli model is used, where local stiffness diameters and material properties are useful to estimate the bending stiffness of the machine. Notably, the stiffness diameters do not necessarily correspond to the physical diameters of the rotor. Adjustments are made in regions with abrupt changes in diameter to mitigate numerical instabilities and refine the model. This tailored stiffness distribution directly influences the rotor critical speeds, mode shapes, and overall dynamic behaviour. The approach followed in this work aligns with best practices in the field of rotordynamics, as discussed in key references such as Muszyńska [35] and Childs [36]. Further details are here neglected for the sake of brevity.

4. Numerical results for thrust bearing forces

In this section the most relevant results regarding the estimation of the fluid dynamic forces in thrust bearings will be presented and discussed.

First, the fluid-dynamic properties of the thrust bearings are estimated for a wide range of operating parameters (external static axial load [1 ÷ 10kN], oil inlet temperature[40 ÷ 75 °C], shaft rotating speed [6000 ÷ 15000 rpm]). The first experimental dataset from [6] is now considered, to show the main results of the applied methodology. Shaft speed is 14000 rpm, oil inlet temperature is 55 °C and axial clearance is 260 μm. For this case study, the applied load on each side of the bearing is varied between 1 and 500kN and an axial clearance of 260 μm. Surface maps of pressure and temperature and flow regime are calculated for both 6-pad and 8-pad thrust bearings. The results for the 6-pad bearing are shown in Fig. 8 while 8-pad bearing in Fig. 9. It is interesting to notice that oil flow regime is mainly laminar, and this excludes excitation forces related to the turbulent motion of the fluid. This outcome is valid also by changing the bearing operating parameters.

Next, the simulation is repeated by evaluating the load at different collar positions. The stiffness force relationship between the applied load and collar position for each side of the bearing is shown in Fig. 10a. The static equilibrium position is identified at the point where the two load curves for the direct and reverse sides intersect, representing the position for which direct and reverse loads are balanced, and bearing pressurization occurs. Once the stiffness force contributions from both sides are combined, the net axial force, for an axial displacement of the collar, is determined as the scalar difference between the two contributions. The resulting net force–displacement relationship for the bearings is displayed in Fig. 10b. The required force for moving the collar, from the equilibrium position towards the reverse or direct side, increases exponentially approaching the pads.

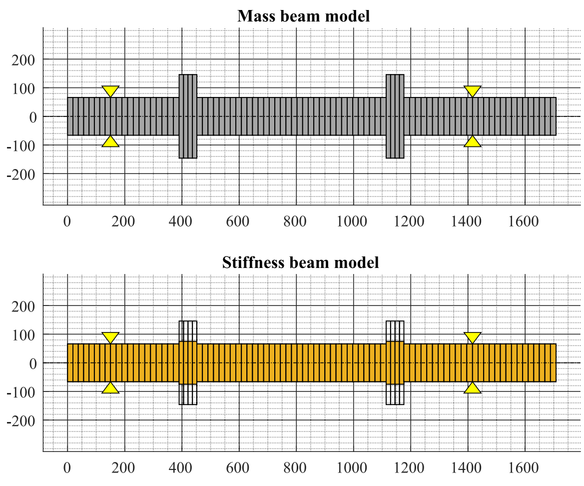

Fig. 7. Finite elements beam model for studying lateral dynamics of the test rig.

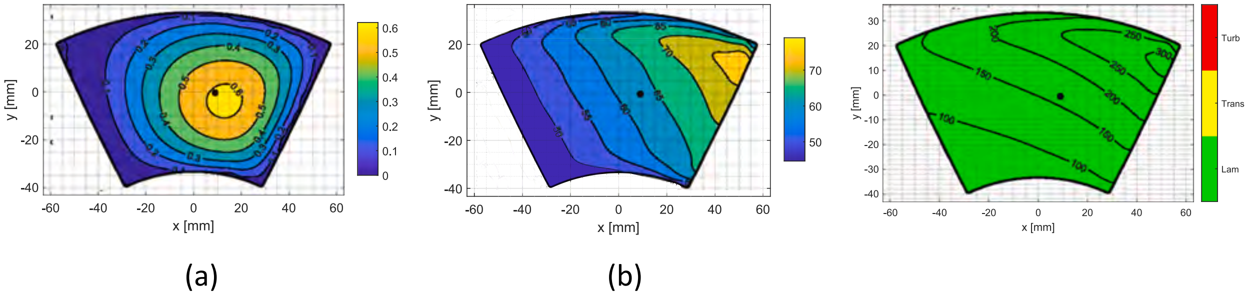

Fig. 8. Computed surface fields for pressure **(a)** temperature **(b)** and flow regime **(c)**, over pad surface for bearing #1, side load 10kN, $\Omega =$ 14000 rpm.

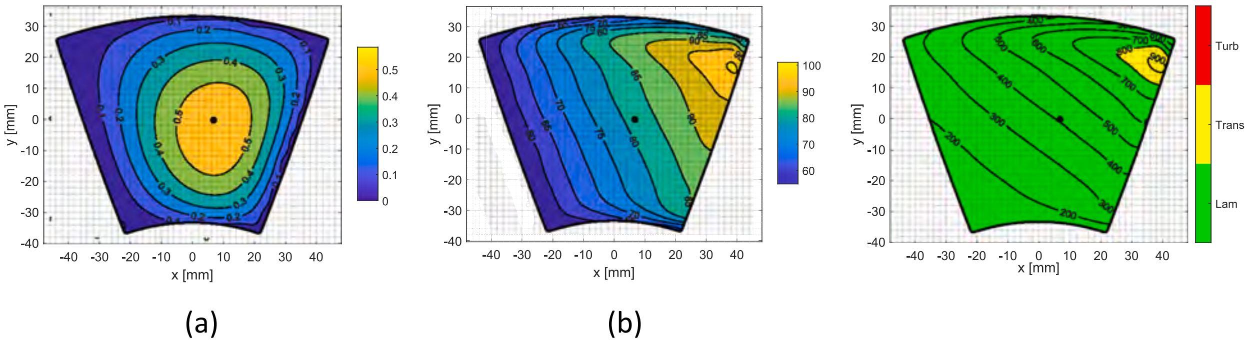

Fig. 9. Computed surface fields for pressure **(a)** temperature **(b)** and flow regime **(c)**, over pad surface for bearing #2, side load 10kN, $\Omega =$ 14000 rpm.

The damping force follows a similar approach. For sake of simplicity, damping force has been considered nonlinear depending on the collar position and linearized for small squeezing velocity values, according to the definition of damping coefficient. The resulting nonlinear damping coefficient trend is shown in Fig. 11. Damping coefficient has a minimum for equilibrium position and then increases exponentially approaching the pads. In this case the coefficient is always positive, since the force direction is given by the scalar product of the coefficient by the vibration velocity vector.

5. Numerical results for axial dynamics and experimental comparison

The most relevant results of the nonlinear axial analysis are here presented and discussed. The nonlinear net force relations from the thrust bearings and the known parameters are inserted in the dynamic equation of motion. The shaft mass, approximately 213 kg, is taken from the literature, while the nonlinear forces from both thrust bearings act as two parallel equivalent springs, meaning their effects are summed up when they are both installed. A similar procedure is applied to the nonlinear damping forces provided by the bearings. For search of general interest, the external acting force is modelled as a single harmonic excitation. The excitation frequency swept across the range $60 \div 270$ Hz. The dynamic force amplitude (approximately 700 N) is adjusted to match the vibration amplitude observed at resonance in the experimental data in [6]. Further considerations about the exciting force are discussed in Sections 5.5 and 5.6.

Several parametrical analyses are performed, by changing one operating parameter of the thrust bearing at a time, namely the static axial load, the oil inlet temperature, the axial clearance, and the shaft rotating speed. Each numerical analysis corresponds to an experimental setup detailed in [6]. When discussing the theoretical findings, well-specified references have been made to the relevant plots in DeCamillo’s work, ensuring a clear and direct comparison between the calculated predictions and the experimental data. We hope that this approach will guide the reader, enabling an easy and intuitive comparison of the main outcomes, and providing a clear validation of the theoretical model through experimental evidence. The complete comparison between numerical and experimental findings is shown in Table 7. Harmonic balance approach is the main method used; while Time integration is only applied in Section 5.6, to better catch the sudden changes in vibration amplitude. For case studies in Section 5.1 both the two thrust bearings are installed to apply the static axial load. For the case studies in Sections 5.2 and 5.3 static axial load is null and only thrust bearing #2 is installed, for Section 5.4 only thrust bearing #1 is installed. All the operating conditions are listed in Table 4.

5.1. Sensitivity to axial static load

First of all, a sensitivity analysis on the static load was performed. Load range is extended from the experimental interval of $0 \div 5$kN in [6], to the interval 0 ÷ 10kN in order to provide a more comprehensive understanding of the system dynamic behaviour. Fig. 12 highlights how the system backbone curve changes with respect to static axial load. At zero load, the axial natural frequency is approximately 127 Hz. However, as the axial load increases, this frequency increases up to 190 Hz. Furthermore, the shape of the backbone curve changes considerably when axial load increases, the bending to the right of the dynamic peak (stiffening behaviour) decreases, and the peak amplitude decreases too. Bi-stability condition always happens when multiple solutions exist for a specific frequency, the bi-stability area is more relevant for low axial load condition.

The same information is now represented in a waterfall plot, as shown in Fig. 13a, where the amplitude of vibration is plotted as a function of the applied static axial load. The curve hight indicates the zero-to-peak vibration amplitude of the system. The results clearly show that the natural frequency increases as the static load is increased.

Fig. 13b represents the same waterfall, shown from the top view for an easy comparison of the numerical and experimental frequencies. The red dashed line represents the axial SSV frequency, observed in the experiments in [6], specifically in Fig. 8 of DeCamillo's study. The attention is given to the "Reducing load" phase where axial SSV is clearly visible at 125 Hz and its frequency shifts with the axial load. The red dashed line represents the frequency trend of the SSV signature in DeCamillo's work. By comparing it with the map crest, the computed axial resonance is very similar to the experimental signature. Finally, the computed vibration amplitude along the red line is extracted by the waterfall and the resulting curve is plotted in Fig. 14. According to nonlinear vibration theory, when the red line intersects the bi-stable region, three potential vibration states arise: one unstable and two stable solutions (with low and high amplitudes). The two stable solutions are shown in Fig. 14, for a static axial load lower than 5.7kN, bi-stability can occur since the two lines are not null. This outcome is confirmed by the experimental measurements from [6]. Moreover, the same experimental data suggests that when bi-stability occurs, abrupt changes between low and high amplitude responses occur, as also discussed in other works [19].

5.2. Sensitivity to axial clearance

The effect of axial clearance of the thrust bearing on the axial dynamics is here addressed. In this case study, only bearing #2 is installed, with a fixed oil inlet temperature of 55 °C and a constant shaft rotational speed of 14,000 rpm. Two values of bearing clearance are considered: 260 μm and 600 μm. As shown in Fig. 15a, increasing the clearance results in a reduced pressurization on both sides of the bearing. As the clearance grows, the net force–displacement curve becomes increasingly nonlinear and less stiff (Fig. 15b).

A significant reduction in axial stiffness is one key consequence of the greater axial clearance, causing the system natural frequency to drop down from 120 Hz to 110 Hz. Additionally, the vibration amplitude for the same applied force is much larger due to the reduced stiffness of the bearing, as shown in Fig. 16. It is also important to note that, like in the previous cases, an experimental SSV is observed in [6] for the larger clearance case (Fig. 10 of DeCamillo's study). Axial SSV is visible at 113 Hz for an oil flow rate of 44gpm. The experimental data closely matches the numerical axial natural frequency range.

5.3. Sensitivity to oil inlet temperature

The effect of oil inlet temperature on fluid dynamic forces is addressed. As oil inlet temperature increases, the mean oil temperature distribution inside the oil wedge increases as well, due to thermal balance. The oil viscosity reduces and consequently also the oil film thickness at pad pivot decreases for a given load. The current model deals with an important simplification. It is assumed that the oil film wedge is fully filled, although in real cases, partial filling and de-pressurization could occur for the highest rotational speeds. Under this hypothesis, both an increase in lubricant flow rate and a reduction in inlet oil temperature have similar effects, as they increase the average oil temperature over the pad surface. In this work, the only variation of inlet oil temperature will be considered for sake of brevity.

For the current case study, only thrust bearing #2 is installed on the test rig, axial clearance is 600 μm, shaft speed is 14,000 rpm and the inlet oil temperature is varied within the range of 45 °C to 75 °C. Fig. 17a shows the effect of inlet temperature on the fluid-dynamic forces generated by the two sides of the bearing. As the inlet temperature increases, the oil film thickness at pivot reduces on both sides, causing a significant drop in pressurization. As shown in Fig. 17b, the thrust bearing force curve becomes increasingly nonlinear with higher inlet temperatures.

Fig. 18 shows the waterfall diagram of the system axial response as a function of oil inlet temperature change. By looking at the numerical results, the axial natural frequency of the test rig is found to be around 110 Hz for an oil inlet temperature of 55 °C. The oil temperature significantly changes the axial natural frequency, the axial natural frequency decreases as the temperature increases. A minimum value of 75 Hz is reached for oil temperature of 75 °C. The red point in Fig. 18 at 113 Hz represents the SSV frequency extracted from experiments in Fig. 10 of DeCamillo's work [6]. For this case study a direct validation is not straightforward since DeCamillo changed and measured the coolant flow rate in the thrust bearing rather than the inlet temperature. As previously discussed, a numerical estimation of the bearing performance correlated to the oil flow rate is quite difficult and it needs for detailed model tuning. Even though inlet oil temperature is used as input parameter to simplify the analysis, there is a good correlation between the experimental findings and the estimated axial natural response. For this case study only the red point datum is available from the experimental data in [6]. The vibration amplitude, extracted across the red dashed line, is shown in Fig. 18. Bi-stability region is found around the triggering temperature (55 °C) for axial SSV. The obtained inlet oil temperature value is a reasonable working condition of the bearing from the practical point of view.

Table 4
Operating conditions for the considered case studies from [6].

Case study	Paper section	Corresponding plot in literature[6]	Parametrical analysis range	Nominal parameters				
				Installed bearing	Axial clearance	Axial load	Oil inlet temperature	Shaft speed
Axial load	5.1	Fig. 8 [6]	0-10kN	BRG 1 + BRG 2	260 μm	0kN	55 °C	14000 rpm
Axial clearance	5.2	Fig. 10 [6]	260–600 μm	BRG 2	600 μm	0kN	55 °C	14000 rpm
Oil temperature	5.3	Fig. 10 [6]	40–75 °C	BRG 2	600 μm	0kN	55 °C	14000 rpm
Shaft speed	5.4	Fig. 11 [6]	6000–15000 rpm	BRG 1	600 μm	0kN	55 °C	9000 rpm

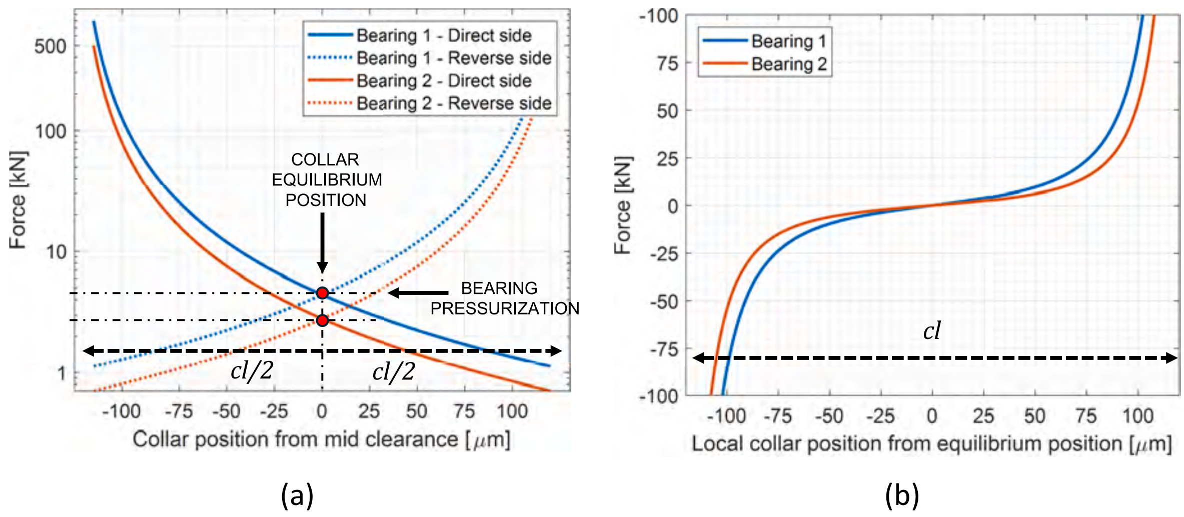

Fig. 10. Fluid dynamic stiffness forces computed for an oil-lubricated double-sided thrust bearings. **(a)** Axial stiffness force contributions from both sides. **(b)** Nonlinear stiffness net force–displacement relationship for bearings #1 and #2, horizontal axis is the collar axial position, clearance 260 μm, $\Omega = 14000$ rpm.

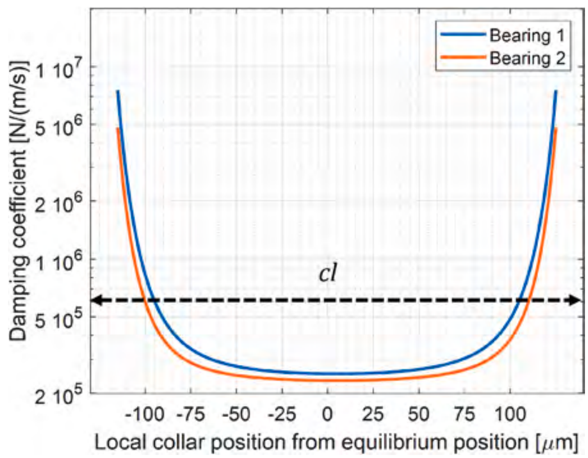

Fig. 11. Nonlinear damping coefficient relationship for bearings #1 and #2, horizontal axis is the collar axial position, clearance 260 μm, $\Omega = 14000$ rpm.

5.4. Sensitivity to rotating speed

The effect of shaft rotating speed is here studied. In this case study only thrust bearing #1 is installed, the axial clearance is 600 μm and the oil inlet temperature is 55 °C. The shaft speed is ranged from 6000 rpm to 15,000 rpm. It is relevant to underly that this analysis is performed as a series of equilibrium conditions and not in transient conditions. This hypothesis is valid since the rotational speed is experimentally slowly changed in time. Fig. 19 represent the new fluid dynamic forces of the bearing. As the shaft speed increases, the pressurization in the bearing also rises and the axial natural frequency of the system increases. The hypothesis of fully filled oil film wedge is assumed, so no reductions in pressurization are considered. The validity of this hypothesis is confirmed by the following experimental outcome. Centrifugal depressurization is measured by pressure probes on the pad surface, and it is found that when depressurization occurs then axial SSV cannot be reproduced on the test rig.

The system sensitivity to the shaft rotating speed is shown in the response map of Fig. 20. It is worth noting that, based on experimental data in Fig. 11 of DeCamillo's work [6], a SSV signature at 95 Hz was observed only at shaft speeds higher than 9000 rpm. This trend is confirmed by the numerical results since at speeds greater than 9000 rpm, the axial SSV frequency aligns with the axial natural frequency, and resonance condition occurs. Also in this case, the single experimental measurement is shown as a red point in Fig. 20a. The vibration amplitude is extracted across the red dashed line and bi-stability condition can occur for rotating speeds higher than 8000 rpm.

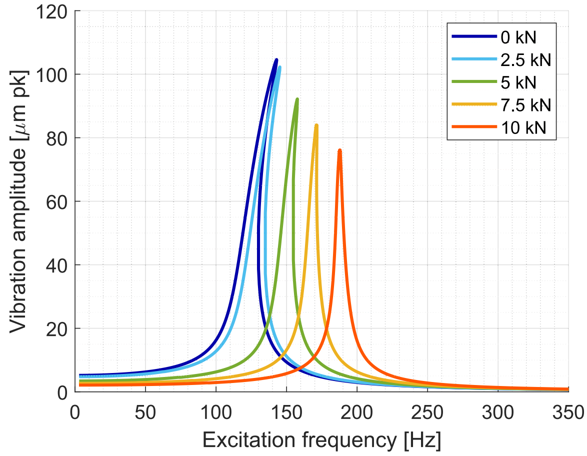

Fig. 12. Backbone curves representing the computed axial dynamic response of the system. Axial load considerably shifts the peak frequency and the curve slope.

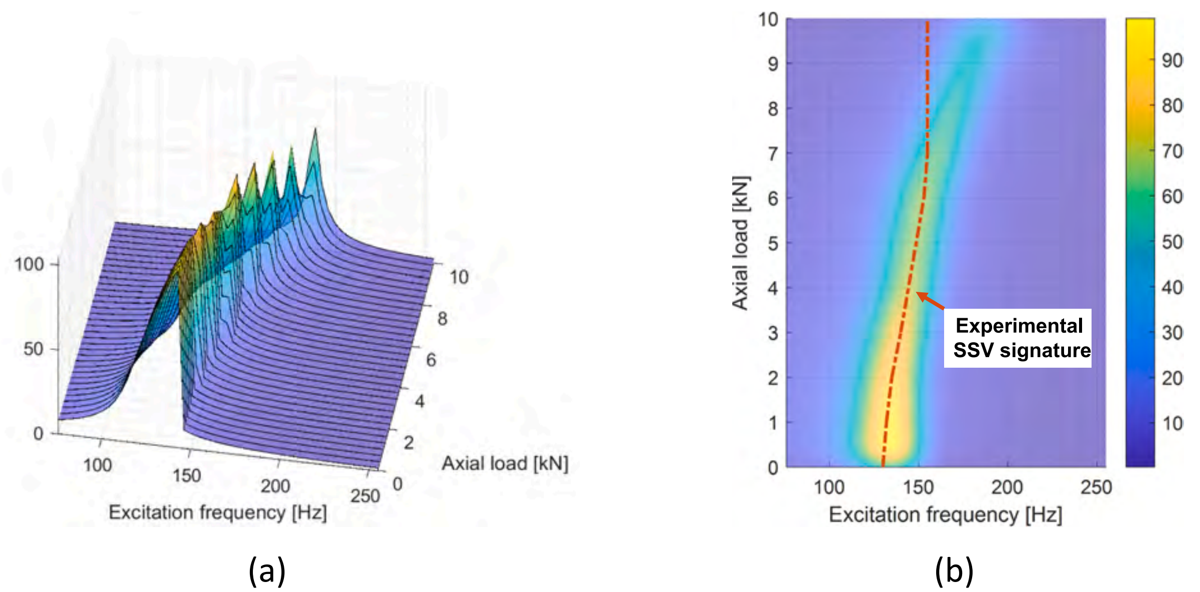

Fig. 13. Dynamic response of the system as a function of the static axial load applied to the thrust bearings. **(a)** Waterfall plot of the maximum system response. **(b)** Top view for comparison between numerical and experimental natural frequency. Axial load 0 ÷ 10kN, clearance 260 μm, Ω = 14000 rpm.

5.5. *Investigation of radial natural frequencies as excitation source*

Radial dynamics of the rotor is here briefly considered to understand if thrust collar lateral vibrations can be a reasonable exciting force for the axial dynamics. It is important to mention that the Finite Element (FE) model used in this study is a simplification, as it does not account for the coupled axial-radial dynamics. Instead, only the tilting stiffness provided by the tilting of the thrust collar ($K^i_{d,r}$) is considered. The tilting stiffness introduced by the two thrust bearings are linearized for the nominal operating condition, which depends on the static axial load, the axial clearance and the shaft speed. Table 5 summarizes the tilting stiffness coefficients for the different case studies. The values are linearized for the nominal operating conditions of the test rig for the different cases, as listed in Table 4.

The bending natural frequencies of the rotor were calculated, and the corresponding Campbell diagram is reported in Fig. 21 for the first case study of Table 4. Particular interest is given to the natural frequencies related to the first (110.7 Hz) and the second (147.5 Hz) vertical bending modes, as they align closely with the experimental axial SSV frequencies measured at 14,000 rpm in the study of DeCamillo [6]. Due to the gyroscopic effect, the first bending mode is associated with the eigenvalues 1,2 while the second bending mode to 3,4. The thrust collar tilting stiffness has an important effect since it increases by 15 % the rotor bending natural frequencies

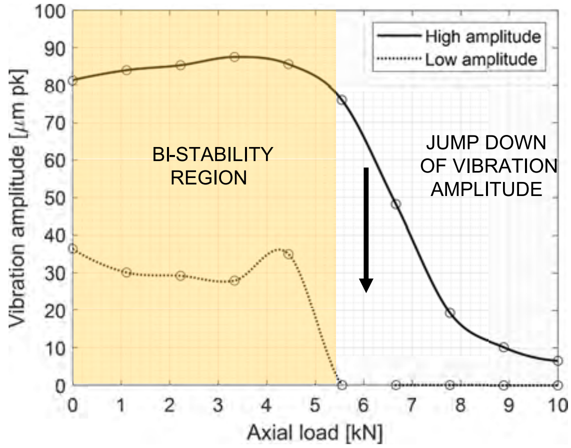

Fig. 14. Numerical estimation of the dynamic response amplitude of the test rig. Vibration amplitude is extracted for an acting force with the same frequency of the experimental data in [6]. Two solutions are present due to bifurcation zone, jump down is highlighted for static axial load higher than 5.7kN.

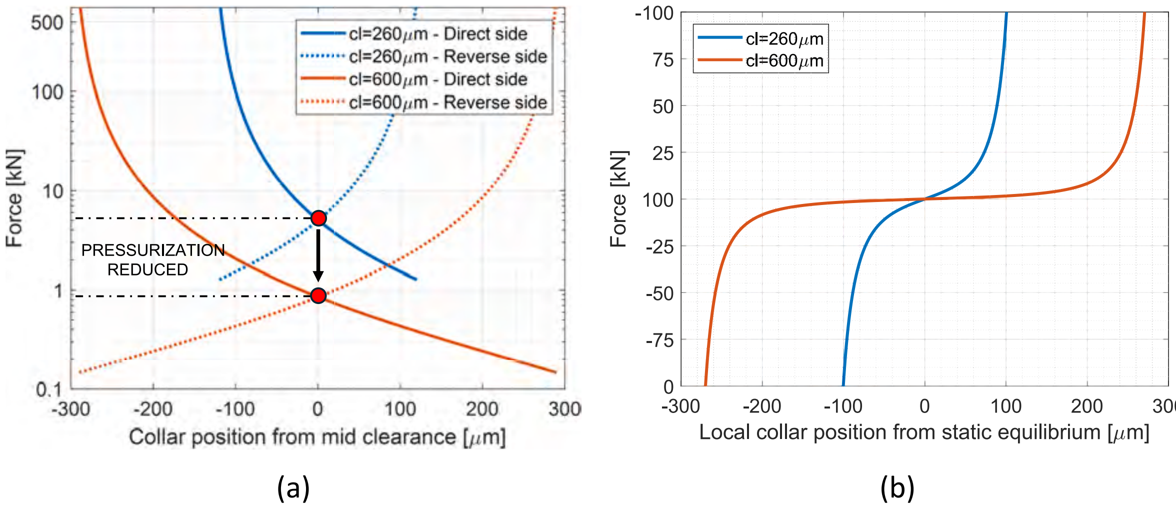

Fig. 15. Fluid dynamic forces computed for an oil-lubricated thrust bearing #2 when changing the axial clearance. **(a)** Axial force contributions from both sides. **(b)** Nonlinear stiffness net force–displacement relationship, horizontal axis is the collar axial position. Clearance 260 μm or 600 μm, oil inlet temperature 55 °C, $\Omega = 14000$ rpm.

(Table 6).

The mode shape corresponding to the first and the second vertical bending modes of the rotor are shown in Fig. 22. The two bending modes cause a significant tilting of both thrust collars. This finding is interesting because it gives a hint about the possible coupling mechanism between radial and axial vibrations. Thus, when the system is excited in radial direction, the same vibration can be seen in axial direction and vice-versa. Also, the rotor static deflection should be considered, because it justifies the misalignment between the surfaces of the collar and the pads.

Table 7 provides a summary of the key results for the different case studies, by comparing: the experimental frequencies of axial SSV, the natural frequencies in the axial direction, and the natural frequencies of the associated bending modes. In all the considered cases, the natural frequencies in axial and radial directions are closely aligned, and in particular the experimental axial SSV frequency is very close to the axial natural frequency of the system. Consequently, dynamic amplification and bi-stability conditions are likely to occur.

5.6. Transient behaviour

The rotor axial dynamics is investigated also in transient conditions. This analysis is particularly useful to catch sudden jumps in vibration amplitudes, that may occur when the axial natural frequency crosses the bi-stability region. The Harmonic balance approach

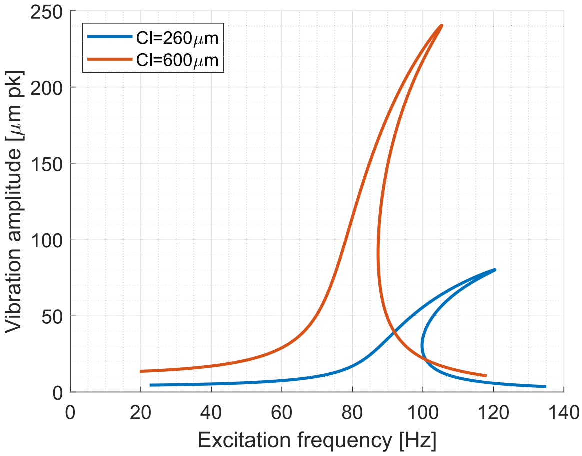

Fig. 16. Backbone curves representing the axial dynamic response of the system as a function of the axial clearance (cl = 260 ÷ 600 μm). An increase of axial clearance reduces the natural frequency of the system and increases the degree of nonlinearity.

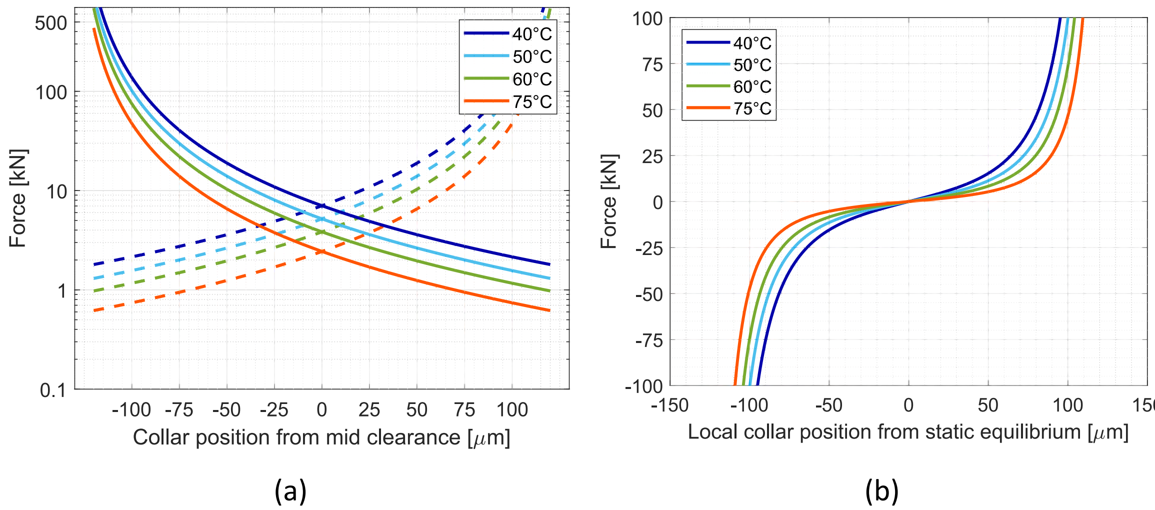

Fig. 17. Fluid dynamic forces computed for oil-lubricated thrust bearing #2 with respect to the oil inlet temperature. **(a)** Axial force contributions from both sides. **(b)** Nonlinear stiffness force–displacement relationship, horizontal axis is the collar axial position. Clearance 600 μm, oil inlet temperature from 45 °C to 75 °C, $\Omega = 14000$ rpm.

is not a suitable solver, since it searches for steady-state solutions. Time integration solver is used even though the computational cost is significantly higher. By using the same machine, Time integration analysis needs approximately 10 times the computational cost of Harmonic balance analysis.

In this analysis the dynamic equilibrium equation of the system is considered, as done previously. The same case-study of Section 5.1 is analysed. The effect of static axial load is considered in time-domain, by using a trapezoidal time law for changing the axial static load in the range 0-10kN, as shown in Fig. 23. The slope of the time ramp is not significant, and it was found not to change the obtained results.

The choice of the dynamic force is useful to investigate the possible excitation sources and their effect on the axial dynamics. To simplify the problem a single harmonic force, with an amplitude of 700 N, is considered as excitation. The simulation is performed for several values of the excitation frequency. The considered excitation sources and the corresponding frequencies are listed in Table 8.

The results of the analysis are shown in Fig. 24, where the rotor axial position is plotted over time for the different excitation frequencies. For each time series, the vibration envelope (peak-to-peak amplitude) is computed and shown in Fig. 25 for an easy comparison.

Several interesting outcomes comes from the numerical results. First of all, nonlinearities are clearly visible for vibration responses of case 2 (110.7 Hz) and case 3 (147.5 Hz). Sudden jumps in the vibration amplitude occur when static axial load is changed, and the axial natural frequency align with the excitation frequency. During the loading and the de-loading ramps hysteresis occurs and the system response is not symmetric. This unpredictable behaviour is the result of the bi-furcation occurrence. Moreover, the Time

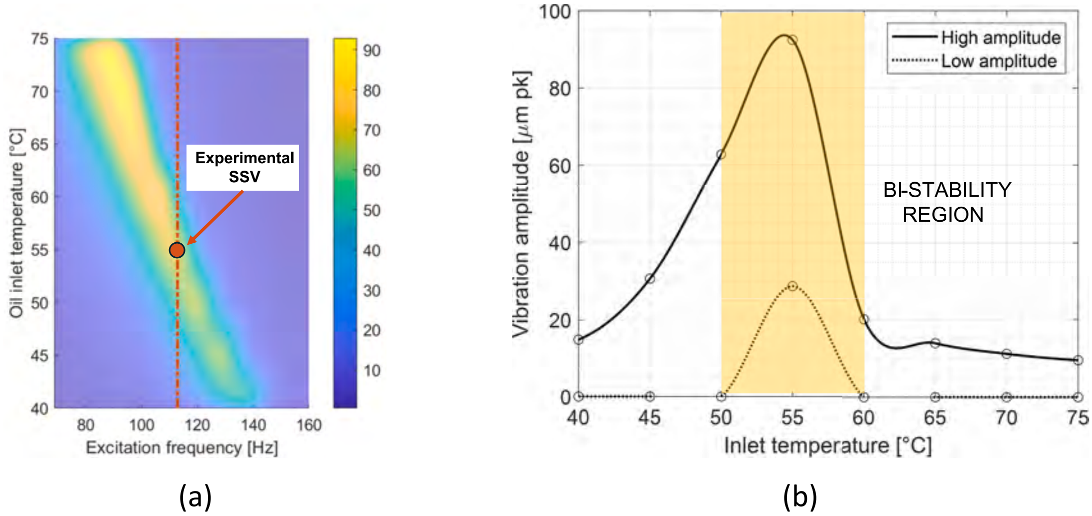

Fig. 18. Dynamic response of the system as a function of the oil inlet temperature at the leading edge of the pads. (a) 2D map of the maximum system response. (b) Vibration amplitude extrapolated for an acting force with the same frequency of the experimental data in [6].

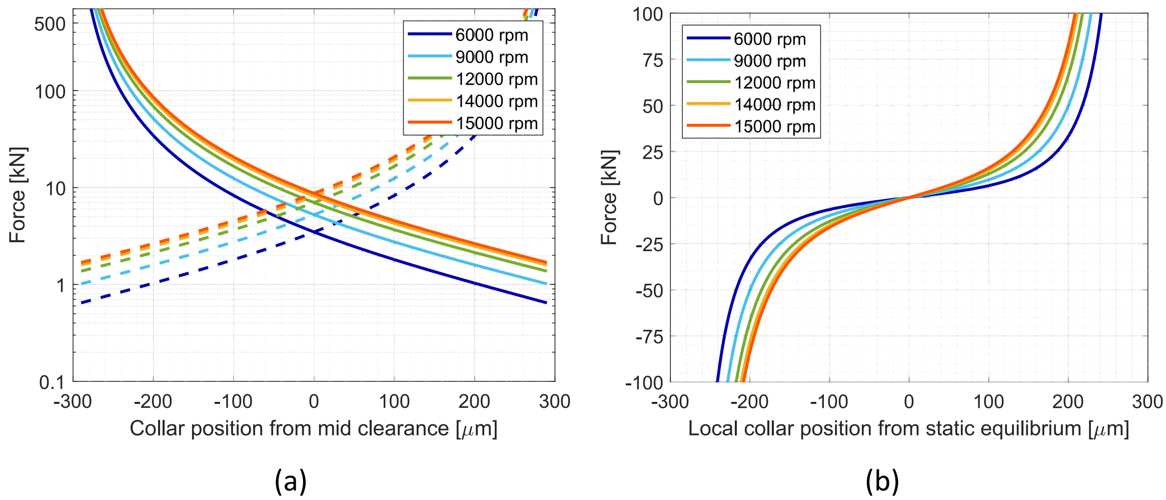

Fig. 19. Fluid dynamic forces computed for oil-lubricated thrust bearing #1 when changing the shaft rotating speed. **(a)** Axial force contributions from both sides. **(b)** Nonlinear stiffness force–displacement relationship, horizontal axis is the collar axial position. Clearance 600 μm, oil inlet temperature 55 °C, rotational speed from 6000 rpm to 15000 rpm.

integration confirms the results of the HB analysis. When looking at the lower and upper limits of the axial natural frequency, no dynamic amplification occurs, and no strange behaviour is obtained. This finding confirms that the system axial natural frequency stays in the range 100–200 Hz, as discussed in Section 5.1.

When looking at excitation frequencies coherent with the synchronous component (233 Hz) no dynamic amplification is seen. This outcome is interesting since it excludes that the syncronous unbalance could excite an axial nonlinear response of the system. Fig. 25 shows the same output as peak-to peak vibration amplitude. By comparing the system response amplitude of the different cases, cases 2 and 3 generate a significant high amplitude (40–160 μm) and nonlinear system behaviour, while cases 1,4,5 excite a negligible and linear system response.

6. Conclusions

This research focuses on the phenomenon of axial sub-synchronous vibrations (SSV) in rotating machinery, which has a significant impact from the industrial point of view. All the analysis are conducted over a well-known case study present in the literature and the proposed methodology can become easily of general interest. The nonlinear forces generated by double-sided oil lubricated thrust bearings have a key role and they can explain the sudden changes in vibration levels often observed in axial SSV signatures. Once they

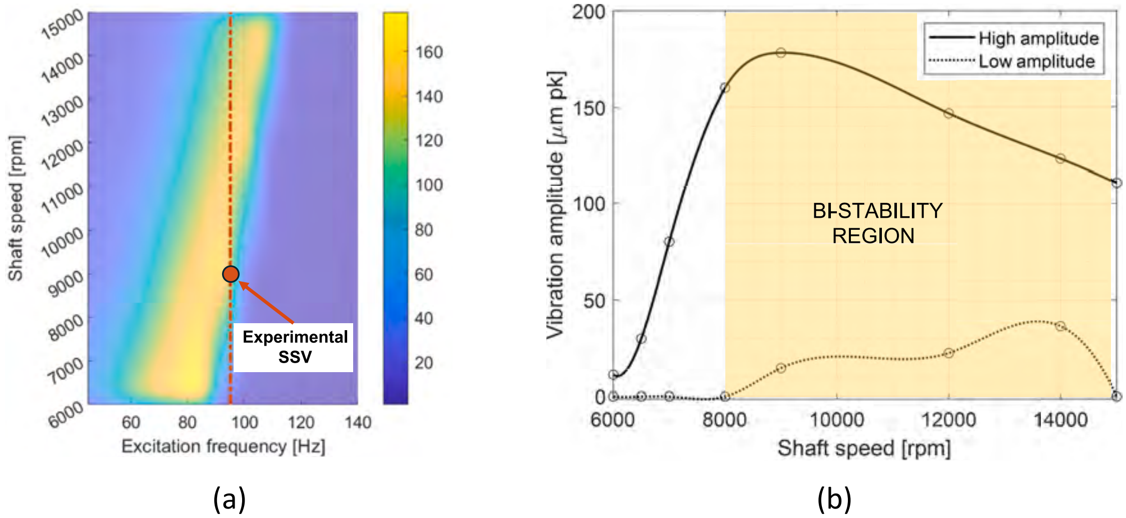

Fig. 20. Dynamic response of the system as a function of the oil inlet temperature at the leading edge of the pads. (a) 2D map of the maximum system response. (b) Vibration amplitude extrapolated for an acting force with the same frequency of the experimental data in [6].

Table 5
Tilting stiffness coefficients for thrust bearing, linearized for the nominal operating conditions.

Case study	Bearing #1	Bearing #2
Axial load	7.1984*10ˆ6 Nm/rad	8.3841*10ˆ6 Nm/rad
Axial clearance	Not installed	6.6413*10ˆ5 Nm/rad
Oil temperature	Not installed	6.6413*10ˆ5 Nm/rad
Shaft speed	3.6608*10ˆ5 Nm/rad	Not installed

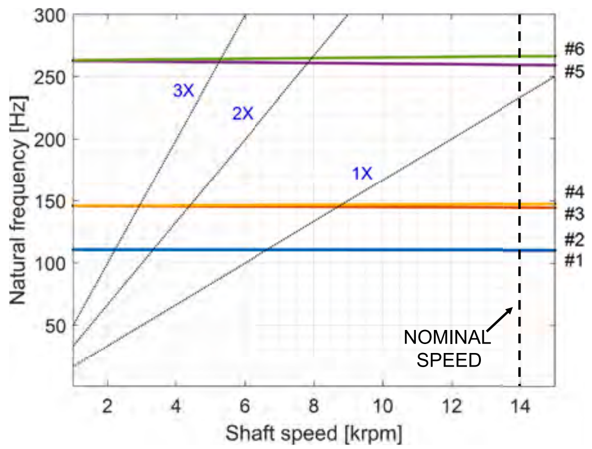

Fig. 21. Campbell diagram for lateral dynamics of the test rig. The thrust bearing tilting stiffness coefficients are calculated from the first case study of Table 4.

Table 6
Natural frequencies of the first two vertical bending modes by considering or neglecting the thrust bearings tilting stiffness coefficients.

	Bending natural frequency w/o tilting stiffness	Bending natural frequency with tilting stiffness
Bending mode #1	103.5 Hz	110.7 Hz
Bending mode #2	118.6 Hz	147.5 Hz

Table 7
Comparison of experimental axial SSV frequency and rotor natural frequencies in both radial and axial directions. Four case studies are considered.

Set of experiments	Installed bearing	Experimental axial SSV [6]	Numerical axial natural frequency	Numerical lateral mode #1	Numerical lateral mode #2
Axial load [0-10kN]	BRG 1 + BRG 2	125–160 Hz	127–190 Hz	110.7 Hz	147.5 Hz
Axial clearance [600 μm]	BRG 2	113 Hz	110 Hz	104.0 Hz	121.9 Hz
Oil temperature [55 °C]	BRG 2	113 Hz	110 Hz	104.0 Hz	121.9 Hz
Shaft speed [9000 rpm]	BRG 1	95 Hz	90–110 Hz	108.1 Hz	118.7 Hz

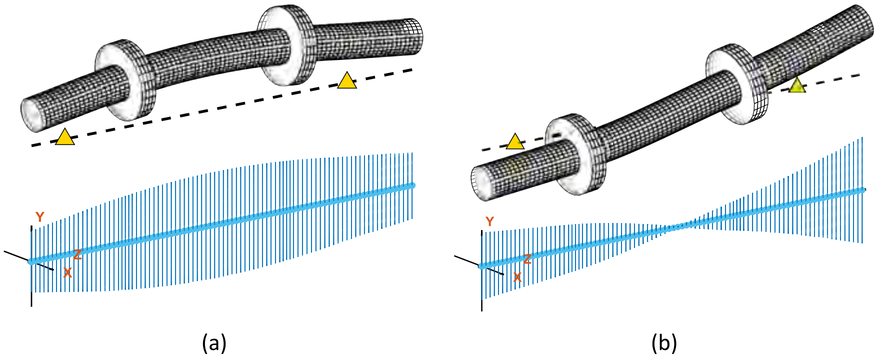

Fig. 22. Sketch of the mode shapes related to the first bending modes of the rotor in vertical direction and nominal speed 14000 rpm. Mode shape #1 **(a)** and mode shape #2 **(b)**.

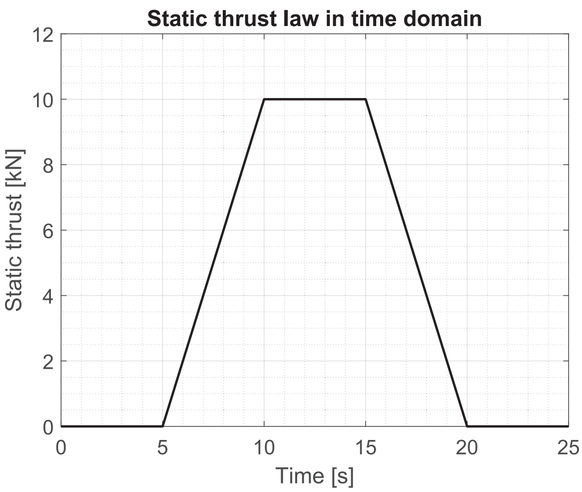

Fig. 23. Trapezoidal law to apply static axial load in time-domain analysis.

Table 8
Possible excitation sources considered in axial direction.

Case study	Excitation phenomenon	Frequency
1	Lower limit of the axial natural frequency from HB	100 Hz
2	Frequency of the first lateral bending mode	110.7 Hz
3	Frequency of the second lateral bending mode	147.5 Hz
4	Upper limit of the axial natural frequency from HB	200 Hz
5	Frequency of synchronous excitation	233 Hz

are calculated, they are used to set up a simplified axial model for the system nonlinear dynamics. The numerical problem is addressed by using Harmonic balance method and Time integration to solve the dynamic equilibrium equation. A sensitivity analysis is conducted to explore how key operating parameters of the thrust bearing, namely static axial load, oil inlet temperature, axial clearance,

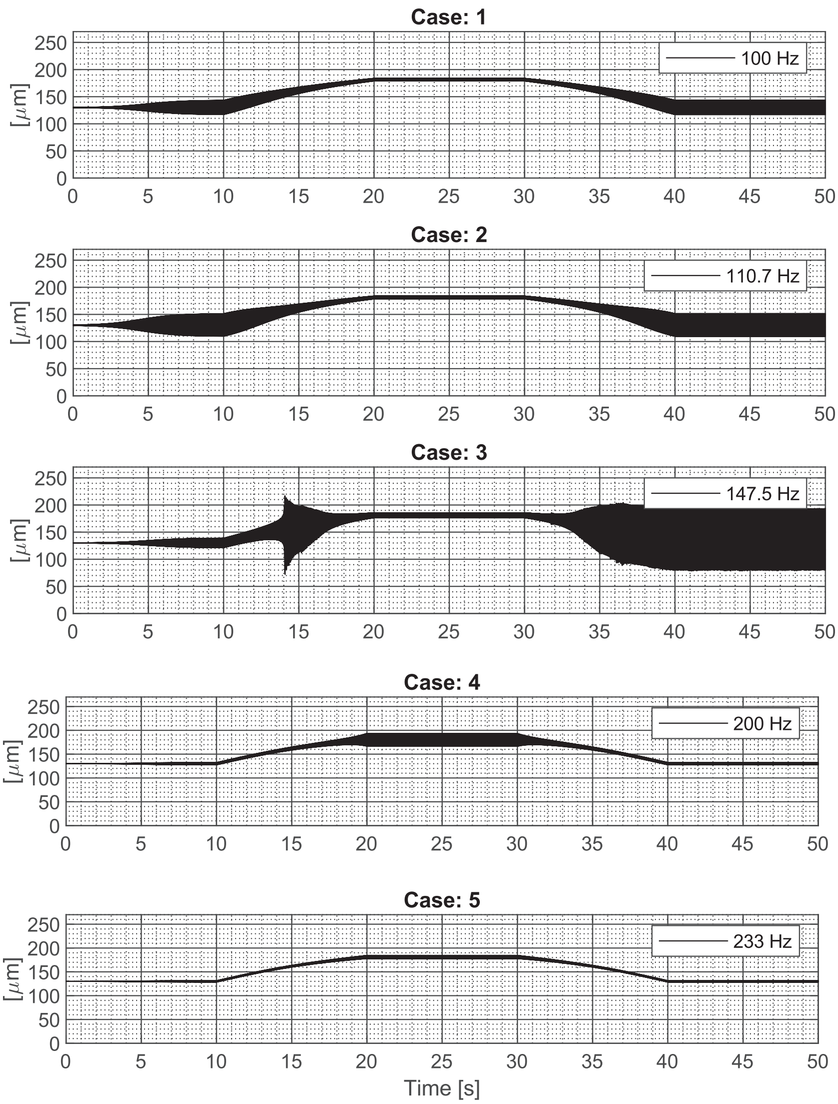

Fig. 24. Rotor absolute axial displacement in time-domain, computed from reverse side for several excitation sources. Non-linearities, sudden jumps up and down in vibration amplitude and hysteretic behaviour are visible when static axial load is changed.

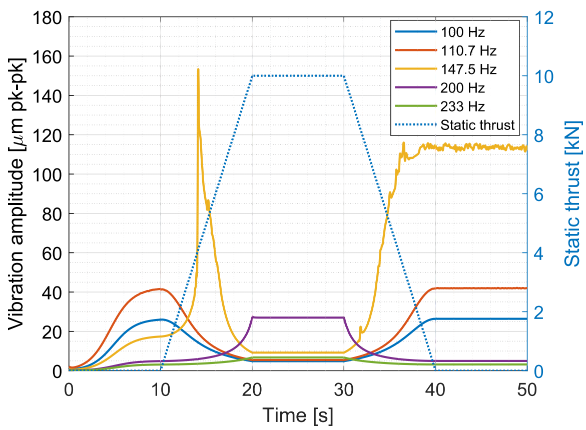

Fig. 25. Envelope of the vibration amplitude for the considered cases (left axis), axial static load (right axis).

and rotor speed, affect the system axial dynamic response.

One interesting topic and already open question is the root cause of the excitation force. By reviewing the literature, the possible coupling between axial and radial dynamics due to the thrust collar seem to be reasonable. Moreover, the model results fit well with experimental data from the literature. In this work, lateral dynamics is briefly analysed, showing that the frequency of experimentally observed sub-synchronous vibrations aligns closely with the natural frequency of the rotor first bending modes. These findings support the existing literature, highlighting the necessity of considering the interaction between lateral and axial dynamics, particularly in machines equipped with thrust collars.

A valuable further improvement of this work would be to develop a fully coupled lateral-axial dynamic model, which could definitively demonstrate the presence of self-excited coupled vibrations in such systems.

CRediT authorship contribution statement

Ludovico Dassi: Writing – review & editing, Writing – original draft, Methodology, Investigation, Formal analysis. **Steven Chatterton:** Writing – review & editing, Software, Methodology, Formal analysis, Data curation, Conceptualization. **Paolo Pennacchi:** Writing – review & editing, Methodology, Funding acquisition, Formal analysis, Conceptualization.

Declaration of competing interest

The authors declare that they have no known competing financial interests or personal relationships that could have appeared to influence the work reported in this paper.

Acknowledgments

The study is founded by the project: Next-GenerationEU (Piano Nazionale di Ripresa e Resilienza - PNRR), mission n°4, component n°2, investment n°3.3, DM 352 of 09/04/2022.

The authors gratefully acknowledge Ansaldo Energia S.p.A. for supporting the work and contributing valuable insights, allowing the publication of this research.

Data availability

The data that has been used is confidential.

References

[1] K. Abudu, U. Igie, I. Roumeliotis, R. Hamilton, Impact of gas turbine flexibility improvements on combined cycle gas turbine performance, Appl. Therm. Eng. 189 (2021) 116703, https://doi.org/10.1016/j.applthermaleng.2021.116703.
[2] Y. Yang, T. Nikolaidis, S. Jafari, P. Pilidis, Gas turbine engine transient performance and heat transfer effect modelling: A comprehensive review, research challenges, and exploring the future, Appl. Therm. Eng. 236 (2024) 121523, https://doi.org/10.1016/j.applthermaleng.2023.121523.
[3] B.A. Silva, A method for the very early detection of rotor-casing rub in aeroderivative gas turbines, Ph.d. Thesis. e.t.s.i. Industriales (UPM) (2021).
[4] Ben Rahmoune M, Iratni A, Hafaifa A, Colak I. Gas Turbine Vibration Detection and Identification based on Dynamic Artificial Neural Networks 2023.
[5] R.G. Kirk, A. Alsaeed, J. Liptrap, Experimental Test Results for Vibration of a High Speed Diesel Engine Turbocharger, Tribol. Trans. 51 (2008) 422–427.
[6] S. DeCamillo, Axial Subsynchronous Vibration (2014), https://doi.org/10.21423/R1K35G.
[7] B.R. Fabijonas, L. Krajewski, A. Hegde, R. Rodzwic, Design Considerations for Directed-Lubrication Thrust Bearings Across a Wide Range of Operating Conditions With a Focus on Pressure Drop in the Oil Supply Path, American Society of Mechanical Engineers Digital Collection (2024), https://doi.org/10.1115/GT2024-126536.
[8] A.-T. Watban Khalid Fahmi, K. Reza Kashyzadeh, S. Ghorbani, A comprehensive review on mechanical failures cause vibration in the gas turbine of combined cycle power plants, Eng. Fail. Anal. 134 (2022) 106094, https://doi.org/10.1016/j.engfailanal.2022.106094.
[9] L.A. Branagan, Survey of Damage Investigation of Babbitted Industrial Bearings, Lubricants 3 (2015) 91–112.
[10] Z.-M. Li, T. Liu, H. Kang, J. Tian, J. Jing, D. Wang, Theoretical and experimental investigations on steady-state responses of rotor-blade systems with varying rotating speeds based on a new nonlinear dynamic model, Mech. Syst. Sig. Process. 184 (2023) 109692, https://doi.org/10.1016/j.ymssp.2022.109692.
[11] T.A. El-Sayed, M.I. Friswell, H. Sayed, Approximating fluid bearing characteristics using polynomials for the nonlinear dynamics of rotating machines, Tribol. Int. 187 (2023) 108669, https://doi.org/10.1016/j.triboint.2023.108669.
[12] W.W. Gardner, An Experimental Study of Thrust Pad Flutter, J. Tribol. 120 (1998) 577–582, https://doi.org/10.1115/1.2834590.
[13] O. Wu, Y. Xiaoyang, J. Qian, Analysis of tilting-pad thrust bearing static instability and lubrication performance under the bistability, Ind. Lubr. Tribol. 66 (2014) 584–592, https://doi.org/10.1108/ILT-08-2012-0069.
[14] A.M. Mikula, R.S. Gregory, A Comparison of Tilting Pad Thrust Bearing Lubricant Supply Methods, J. Lubr. Technol. 105 (1983) 45, https://doi.org/10.1115/1.3254542.
[15] T.F. Peixoto, K.L. Cavalca, Influence of thrust bearings in lateral vibrations of turbochargers under axial harmonic excitation, 12th Int., CRC Press, Conf. Vib. Rotating Mach, 2020.
[16] L. Ishimoto, R. Marques, Radial Subsynchronous Vibration Caused by Axial Vibration, Turbomachinery, Laboratory (2019).
[17] A. Chasalevris, J.-C. Louis, Evaluation of Transient Response of Turbochargers and Turbines Using Database Method for the Nonlinear Forces of Journal Bearings, Lubricants 7 (2019) 78, https://doi.org/10.3390/lubricants7090078.
[18] P. Koutsovasilis, Automotive turbocharger rotordynamics: Interaction of thrust and radial bearings in shaft motion simulation, J. Sound Vib. 455 (2019) 413–429, https://doi.org/10.1016/j.jsv.2019.05.016.
[19] I. Chatzisavvas, A. Boyaci, P. Koutsovasilis, B. Schweizer, Influence of Hydrodynamic Thrust Bearings on the Nonlinear Oscillations of High-Speed Rotors, J. Sound Vib. 380 (2016), https://doi.org/10.1016/j.jsv.2016.05.026.
[20] N. Mittwollen, T. Hegel, J. Glienicke, Effect of Hydrodynamic Thrust Bearings on Lateral Shaft Vibrations, J. Tribol. 113 (1991) 811–817, https://doi.org/10.1115/1.2920697.

[21] M. Mousavi, A. Chaibakhsh, A. Jamali, M. Kordestani, M. Saif, A New Fault Diagnosis Approach for Heavy-Duty Gas Turbines, IEEEASME Trans Mechatron 27 (2022) 3339–3349, https://doi.org/10.1109/TMECH.2021.3138834.
[22] H. Dongxu, D. Xingjian, L. Wen, Z. Yangli, Z. Xuehui, C. Haisheng, et al., A review of flywheel energy storage rotor materials and structures, J Energy Storage 74 (2023) 109076, https://doi.org/10.1016/j.est.2023.109076.
[23] X. Dai, K. Wei, X. Zhang, Analysis of the Peak Load Leveling Mode of a Hybrid Power System with Flywheel Energy Storage in Oil Drilling Rig, Energies 12 (2019) 606, https://doi.org/10.3390/en12040606.
[24] Y. Lie, R. Bhat, Coupled Dynamics of a Rotor Journal Bearing System Equipped with Thrust Bearings, Shock Vib. 2 (1995) 1–14, https://doi.org/10.1155/1995/602701.
[25] D. Kiuchi, Coupled Sub-Synchronous Vibration of Lateral and Axial Directions, Turbomachinery, Laboratory (2011).
[26] M. Krack, J. Gross, Harmonic Balance for Nonlinear Vibration Problems | SpringerLink, Springer-Cham (2019).
[27] M. Geradin, Mechanical Vibrations: Theory and Application to Structural Dynamics, John Wiley and Sons, 2018.
[28] Singiresu S. Rao. Mechanical Vibrations. Third edition. Addison-Wesley Publishing Company; 1995.
[29] P. Alevras, S. Theodossiades, H. Rahnejat, On the dynamics of a nonlinear energy harvester with multiple resonant zones, Nonlinear Dyn. 92 (2018) 1271–1286, https://doi.org/10.1007/s11071-018-4124-2.
[30] L.F. Shampine, M.W. Reichelt, The MATLAB ODE Suite, SIAM J. Sci. Comput. 18 (1997) 1–22, https://doi.org/10.1137/S1064827594276424.
[31] J.M. Wendlandt, J.E. Marsden, Mechanical integrators derived from a discrete variational principle, Phys Nonlinear Phenom 106 (1997) 223–246, https://doi.org/10.1016/S0167-2789(97)00051-1.
[32] M. Redmann, S. Riedel, Runge-Kutta Methods for Rough Differential Equations, J Stoch Anal 3 (2022), https://doi.org/10.31390/josa:3.4.06.
[33] J.J. Wilkes, S.M. DeCamillo, M.J. Kuzdzal, Evaluation of a High Speed, Light Load Phenomenon in Tilting-Pad Thrust Bearings, Proc. 29th Turbomach. Symp., (2000).
[34] A.M. Mikula, The Leading-Edge-Groove Tilting-Pad Thrust Bearing: Recent Developments, J. Tribol. 110 (1985).
[35] A. Muszynska, Rotordynamics, CRC Press, Boca Raton, 2005.
[36] D. Childs, Turbomachinery Rotordynamics: Phenomena, Modeling, and Analysis|Wiley, Wiley, 1993.